Monthly Notices of the ROYAL ASTRONOMICAL SOCIETY

MNRAS **529,** 1321–1332 (2024) https://doi.org/10.1093/mnras/stae542
Advance Access publication 2024 February 20

ExoMol line lists – LV: hyperfine-resolved molecular line list for vanadium monoxide ($^{51}V^{16}O$)

Charles A. Bowesman,[1] Qianwei Qu ,[1,2] Laura K. McKemmish ,[3] Sergei N. Yurchenko [1] and Jonathan Tennyson [1]★

[1]*Department of Physics and Astronomy, University College London, Gower Street, WC1E 6BT London, UK*
[2]*Paul Scherrer Institut, CH-5232 Villigen, Switzerland*
[3]*School of Chemistry, University of New South Wales, 2052, Sydney, Australia*

Accepted 2024 February 16. Received 2024 February 16; in original form 2024 January 3

ABSTRACT

The new hyperfine-resolved HyVO line lists for vanadium monoxide ($^{51}V^{16}O$) are presented. The new line list considers 15 electronic states and comprises almost 59 billion transitions between 3.4 million energy levels, up to 45 000 cm^{-1}. Empirical energy levels obtained through the MARVEL procedure are used to update calculated values to experimental accuracy, making the line list well suited for high-resolution experiments. Machine learning is utilized to refine the energies of levels in important bands, where empirical values are not known. These updates allow for the accurate prediction of line positions in regions of astrophysical interest, particularly in strong rovibronic bands in the infrared and visible. Previously published *ab initio* transition dipole moment curves are adjusted based on experimental lifetime measurements, resulting in increased intensities in key regions. The line list covers levels up to $F = 150$ and is complete up to 5400 K, making it well suited for studies of ultra-hot Jupiter and M-type stellar atmospheres where VO is believed to be a strong source of opacities. The full line list is made available via www.exomol.com.

Key words: molecular data - opacity - planets and satellites: atmospheres - planets and satellites: exoplanets - stars: atmospheres.

1 INTRODUCTION

Vanadium monoxide (VO) is known to exist in cool dwarfs due to its strong absorption spectra, where it is primarily observed in the near infrared (Keenan & Schroeder 1952; Spinrad & Younkin 1966; Wing, Spinrad & Kuhi 1967; Spinrad & Wing 1969; Kirkpatrick, Henry & McCarthy 1991; Cushing, Rayner & Vacca 2005; Lançon et al. 2007; Rajpurohit et al. 2012; Liimets et al. 2022) and visible regions (Kamiński, Schmidt & Tylenda 2010; Tylenda et al. 2011; Loebman et al. 2014; Rajpurohit et al. 2014) through rovibronic transitions. It has also been observed in the envelopes of supergiants (Fawley 1977), red hypergiants such as VY CMa (Wallerstein 1971; Humphreys et al. 2019; Dinh-V-Trung et al. 2022), asymptotic giant branch stars such as VX Sgr (Lockwood & Wing 1982), Mira variables (Merrill, Deutsch & Keenan 1962; Wing & Lockwood 1973; Castelaz, Luttermoser & Piontek 2000; Goranskii & Barsukova 2007; Kamiński et al. 2009; Tylenda et al. 2011), in circumstellar gas around protostars (Hillenbrand et al. 2012) and in protoplanetary discs (Ali-Dib et al. 2014).

VO is expected to be present in and significantly influence the physics of the atmospheres of hot and ultra-hot Jupiter exoplanets (Showman et al. 2009; Gandhi & Madhusudhan 2019; Coulombe et al. 2023), but controversies remain about its detection. In these atmospheres, models suggest VO acts as a driver of thermal inversions at high altitudes (Hubeny, Burrows & Sudarsky 2003; Fortney et al. 2008; Lothringer, Barman & Koskinen 2018) and in both brown dwarfs and exoplanets, it is believed to be a strong source of opacities (Sharp & Burrows 2007). Other studies argue that atmospheric cold traps could instead lead to the depletion of VO from the upper atmospheres (Spiegel, Silverio & Burrows 2009), though this may not be the case in hotter atmospheres (Haynes et al. 2015; Evans et al. 2016). It is believed to be present in the likes of WASP-121b (Evans et al. 2018; Tsiaras et al. 2018; Goyal et al. 2020), WASP-18b (Coulombe et al. 2023) and HD 209458b (Désert et al. 2008; Showman et al. 2009; Schwarz et al. 2015) due to low-resolution studies, with the detection of atomic vanadium suggesting it is available to form gaseous species such as VO (Hoeijmakers et al. 2020); others suggest the presence of atomic Vanadium implies the VO has undergone thermal dissociation (Ben-Yami et al. 2020).

The current best line list data for VO has struggled to facilitate high-resolution detections due to the lack of explicit inclusion of experimentally-derived MARVEL (measured active vibration-rotation energy levels) energy levels and the neglect of hyperfine splitting. A line list for VO was produced by McKemmish, Yurchenko & Tennyson (2016b) based on earlier *ab initio* calculations (McKemmish, Yurchenko & Tennyson 2016a). Dubbed the VOMYT line list after the author's initials, this line list had failed to provide a high-resolution detection of VO in an exoplanet atmosphere (Hoeijmakers et al. 2020; Merritt et al. 2020, 2021; de Regt et al. 2022; Johnson et al. 2023) until a recent study of WASP-76b (Pelletier et al. 2023). One metric for assessing the accuracy of a line list is to

★ E-mail: j.tennyson@ucl.ac.uk

consider the resolving power at which the size of the known observed minus calculated (obs.-calc.) differences of rovibronic line positions will become clearly resolvable. In the case of the VOMYT line list, inconsistencies between the calculated line positions and their measured counterparts are resolvable at $R = 22\,000$ for half of all experimentally measured transitions. Another contributing factor to these non-detections is likely the omission of hyperfine couplings from the spectroscopic model, and, hence, no hyperfine splittings in the spectra generated from it. Hyperfine effects are believed to be important in VO, splitting spectral lines into multiple hyperfine components, which in extreme cases can be separated by more than $0.5\,\mathrm{cm}^{-1}$ and considerably change the structure of observed line profiles. These effects are due to the large nuclear spin on the ^{51}V atom of $I = \frac{7}{2}$ and due to it having one of the largest magnetic dipole moments of any stable nucleus (Stone 2005). As such, proper treatment of hyperfine effects is necessary to produce a VO line list well suited to a versatile range of high-resolution studies.

The spectrum of VO has some similar characteristics to that of TiO, with the strongest features of both occupying nearby wavelength regions. Yet TiO has been firmly detected in exoplanet WASP-189b by Prinoth et al. (2022), while detections of VO remain contentious. While several isotopes of Ti can be detected astronomically (Pavlenko et al. 2020), the dominant isotope is ^{48}Ti, which has zero nuclear spin. This means that ^{48}Ti^{16}O has no nuclear spin and hence no hyperfine splitting effects in its spectrum; as a result, the ToTo TiO line list produced as part of the ExoMol project by McKemmish et al. (2019) is much better suited to high-resolution studies than its sister VOMYT VO line list. Additionally, the ToTo TiO line list incorporated empirical MARVEL energies, whereas the VOMYT line list did not.

Recent work has produced a MARVEL spectroscopic network of the experimental transition data for VO (Bowesman et al. 2022). Building on recent variational models (Qu, Yurchenko & Tennyson 2022b, 2023), we present here a hyperfine-resolved line list for VO that covers 15 electronic states, based on the hyperfine-resolved spectroscopic model of Bowesman, Yurchenko & Tennyson (2023a) and computed using the variational nuclear motion program DUO (Yurchenko et al. 2016), as updated by Qu, Yurchenko & Tennyson (2022a) to allow for hyperfine effects. The new line list is refined with experimentally derived empirical energy levels and is suitable for use in high-resolution spectroscopic studies.

Section 2 outlines the techniques to refine the energy levels of the new VO spectroscopic model to create a hybrid line list. Section 3 details the scope of the new line list and the spectra generated from it. Section 4 provides some discussion on the accuracy of the new line list and its suitability for high-resolution studies. Section 5 presents our conclusions and some paths for future improvements on the work presented here.

2 METHOD

The new spectroscopic model of Bowesman, Yurchenko & Tennyson (2023a) describes 13 of the electronic states that have been observed in transitions: X $^4\Sigma^-$, A′ $^4\Phi$, A $^4\Pi$, B $^4\Pi$, C $^4\Sigma^-$, D $^4\Delta$, 1 $^2\Delta$, 1 $^2\Sigma^+$, 1 $^2\Phi$, 1 $^2\Pi$, 2 $^2\Pi$, 2 $^2\Delta$, and 3 $^2\Delta$. Two additional 'dark' states, 1 $^2\Sigma^-$ and 1 $^2\Gamma$, that are known to exist through *ab initio* calculations and through their spin-orbit couplings to other states are also included. An illustration of these electronic states and their energies is given in Fig. 1, along with the observed electronic bands. This model was used to calculate the term energies for all hyperfine-resolved rovibronic levels in these electronic states below $45\,000\,\mathrm{cm}^{-1}$ and with $F \leq 150$, and in turn the transition probabilities

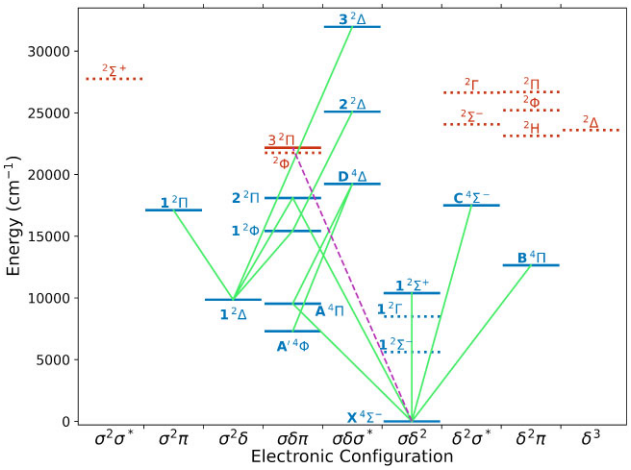

Figure 1. Electronic states of ^{51}V^{16}O and the observed transitions between them arranged based on their dominant electron configuration. States marked in blue are included in the new line list, and those in red are not. States marked with a solid horizontal line are known from experiment, while those marked with a dotted line are from *ab initio* calculations. The 3 $^2\Pi$ state was observed by Hopkins, Hamilton & Mackenzie (2009) through 3 $^2\Pi$–X $^4\Sigma^-$ bands that are unassigned and are marked in purple. Energies for the unobserved, *ab initio* doublets are taken from the calculations of Hübner, Hornung & Himmel (2015).

for all possible transitions between these levels. Hyperfine coupling terms were included in the model for the X $^4\Sigma^-$, B $^4\Pi$, and C $^4\Sigma^-$ states as their hyperfine-resolved energy levels were well studied through experiments (Hocking, Merer & Milton 1981; Cheung, Hansen & Merer 1982a; Suenram et al. 1991; Adam et al. 1995; Flory & Ziurys 2008; Döring et al. 2022) and MARVEL analysis (Bowesman et al. 2022; McKemmish et al. 2024). This set of energy levels and transitions are used as the basis for the states and trans-file components of a new line list. Further refinement is carried out through the MARVELization of the energy levels and the use of machine learning to predict obs.-calc. shifts, resulting in a new, hybrid line list for ^{51}V^{16}O.

2.1 Transition dipole moments

To compute the Einstein A coefficients contained in the trans file portion of the line list, required to calculate intensities, the original dipole moment curves of McKemmish, Yurchenko & Tennyson (2016a) calculated using the program MOLPRO (Werner et al. 2015, 2020) were used. The transition dipole moment curves were initially kept the same, though after calculating final state lifetimes for the new line list there was disagreement between the calculated lifetimes of the A $^4\Pi$, B $^4\Pi$, and C $^4\Sigma^-$ states and the experimental measurements made by Karlsson et al. (1997). These measurements only concerned the lifetimes of $v = 0$ levels in these electronic states and the $v = 1$ levels in the B $^4\Pi$ and C $^4\Sigma^-$ states. Accordingly, there was not sufficient information to fully refit the dipoles. Instead, the transition dipole moments between these three states and the X $^4\Sigma^-$ ground state were scaled. This involved multiplying these three *ab initio* dipole moment curves by scalar values, taken as the square root of the ratio between the calculated lifetimes and the experimental lifetimes for each state. While these states can transition to states other than the ground state, the A $^4\Pi$–X $^4\Sigma^-$, B $^4\Pi$–X $^4\Sigma^-$, and C $^4\Sigma^-$–X $^4\Sigma^-$ bands are the primary decay channels for each of the upper states, as evidenced by being the three strongest electronic

bands in the spectra of VO. The dipoles for each of these bands were scaled by factors of 1.94, 1.58, and 1.33, respectively, and can be found in the Duo input file included in the supplementary material.

The final intensity distributions in the spectra generated from the new line list will differ for two additional reasons. Firstly, the dipole moment curves in the VOMYT model (McKemmish, Yurchenko & Tennyson 2016b) had mistakenly been entered in Λ-representation rather than the Cartesian form appropriate for Molpro outputs. This has been corrected and results in an increase in the intensities of transitions between upper and lower states, both with $\Lambda \geq 1$ and $\Delta\Lambda = \pm 1$ by a factor of 2 (Whiting et al. 1980). Secondly, the spin-orbit coupling curves were refined in an earlier work (Bowesman, Yurchenko & Tennyson 2023a) and allow for intensity borrowing between states, proportional to the magnitude of the coupling. The change in the strengths of these couplings should result in a slight shift in the distribution of intensities between electronic bands.

2.2 MARVELization

Although the parameters of the spectroscopic model were refined against the empirical energy levels determined in a MARVEL study on VO (Bowesman et al. 2022), the final calculated energies do not exactly reproduce the empirical term values. Because of this, one of the final, post-processing steps in the refinement of the line list is to MARVELize the energy levels; where energy levels are known empirically via MARVEL, the energies calculated by Duo are replaced with those from MARVEL. Similarly, the uncertainties determined for these term energies by the MARVEL procedure are taken to be the final uncertainties for these levels. This process has been performed during the refinement of other diatomic, triatomic, and polyatomic molecular line lists to further improve the reproduction of experimental data (Al-Derzi et al. 2021; Mellor et al. 2022; Owens et al. 2022a, 2022b; Semenov, Tennyson & Yurchenko 2022; Yurchenko et al. 2022; Bowesman et al. 2023b).

The MARVEL data set used in this work consists of 5702 hyperfine-resolved and 4712 hyperfine-unresolved energy levels, derived from experimental transitions from 15 sources (Lagerqvist & Selin 1957; Hocking, Merer & Milton 1981; Cheung, Hansen & Merer 1982a; Cheung, Taylor & Merer 1982b; Merer et al. 1987; Suenram et al. 1991; Cheung et al. 1994; Adam et al. 1995; Karlsson et al. 1997; Ram et al. 2002; Ram & Bernath 2005; Flory & Ziurys 2008; Sriramachandran et al. 2008; Hopkins, Hamilton & Mackenzie 2009; Döring et al. 2022).

2.3 Predicted shifts

The MARVEL data for a given vibrational level within an electronic state is sometimes incomplete, with experimental transitions to some F values missing. Where this was the case, a series of fits to the known obs.-calc. values as a function of F were performed to predict synthetic obs.-calc. shifts. Given that the obs.-calc. trends were slightly different for each hyperfine component, the fits were also performed as a function of $F - J$. These fits were carried out over every combination of electronic state, vibrational quantum number, fine structure component, and parity for which MARVEL energies existed. Within each of these combinations, linear regression was performed in multiple segments over the missing data, such that a fit was done over the known obs.-calc. values of between 10 and 15 sequential F values, either side of the missing data. The number of data points, either side was varied to ensure that the linear approximation to the trend in the obs.-calc. data held, as this is only true over small number of F values. A Huber loss algorithm (Owen 2007; Huber & Ronchetti 2009; Pedregosa et al. 2011) was utilized to reduce the sensitivity of the fits to outliers, such as when the variance in obs.-calc. values can become larger for levels involved in electronic state crossings. This interpolation avoids discontinuities between the MARVELized and calculated data and has been employed in the production of other high-resolution line lists (Bowesman et al. 2021; McKemmish et al. 2024).

Uncertainties for levels adjusted with predicted shifts were set to the sum of the mean of the uncertainty in the data included in the linear regression segment and the standard error of the regression,

$$\Delta\tilde{E}_{\rm PS} = \sum_{i=1}^{n} \frac{\Delta\tilde{E}_i + \left|\delta_i - \delta_i^{\rm pred}\right|}{n}, \quad (1)$$

where n is the number of obs.-calc. data points in the fit, $\Delta\tilde{E}_i$ is the uncertainty in a given MARVEL energy from which an obs.-calc. value is calculated, δ_i a singular obs.-calc. value and $\delta_i^{\rm pred}$ its value predicted by the regression model. By using the error in the known obs.-calc. data points, and the error in how well the model predicts those values, we ensure that the estimated uncertainty in the predicted shift energies is on the same order, though slightly worse, than that of the MARVEL energies.

For levels with values of F above the maximum MARVEL value that exists in the band being fit to, $F_{\rm max}$, a similar correction is performed. These levels have an energy shift applied equal to the mean obs.-calc. difference in the final few MARVEL data points in that band. The number of data points over which this mean is taken is generally the same number as used for the regression model segments, but also excludes any data points that lie more than two standard deviations away from the mean. The uncertainty for levels shifted in this manner depends initially on the standard deviation of the obs.-calc. values over which the mean was taken, σ_δ, and is then scaled as a function of F. This scaling is a function of how far this shift has been extrapolated beyond the $F_{\rm max}$ value in the band, taking $F_{\rm ext} = F - F_{\rm max}$ such that

$$\Delta\tilde{E}_{\rm PS} = \sigma_\delta + aF_{\rm ext}(F_{\rm ext} + 1), \quad (2)$$

where a is a constant used to scale the uncertainty, chosen here as $0.0001\,{\rm cm}^{-1}$.

2.4 Calculated levels

For levels without a corresponding MARVEL or predicted shift energy, the energy calculated by Duo is retained. In this case, an estimate for the uncertainty is extrapolated from the mean obs.-calc. energy difference,

$$\Delta\tilde{E}_{\rm Ca} = \Delta\tilde{E} + aF(F+1) + bv, \quad (3)$$

where $\Delta\tilde{E}$ is the mean obs.-calc. energy difference of MARVEL energies in the same electronic state as the calculated level, or the global mean obs.-calc. energy difference if no MARVEL data exists for the corresponding level's electronic state. a and b are constant values used to scale how the estimated uncertainty increases as a function of F and v; the values $a = 0.001\,{\rm cm}^{-1}$ and $b = 0.05\,{\rm cm}^{-1}$ were used.

In cases where calculated energies were replaced with MARVEL or predicted shift energies, the original calculated term energies are retained in the final column of the states file.

3 RESULTS

3.1 New line list

A new line list, consisting of a state file and series of trans files, is now made available and is formatted following the ExoMol standard (Tennyson, Hill & Yurchenko 2013). The states file consists of a series of term energies with associated uncertainties, each with a rigorous F and +/− total parity assignment and labelling for other identifiers such as electronic state, vibrational band, and J. These latter quantum number labels are provided based on the largest contributions to the wavefunction for each state as computed by Duo. An excerpt from the new state file is provided in Table 1. While the fourth column in the ExoMol standard is usually J and g_{tot} is calculated as $(2J + 1) \times g_{ns}$, under hyperfine coupling, the rigorous quantum number is instead F and $g_{tot} = 2F + 1$. This is in keeping with the HITRAN format (Simeckova et al. 2006), such that the total degeneracy of the hyperfine-unresolved level is recouped through the combination of the degeneracies of the individual hyperfine-resolved components. The fifth and sixth columns contain the uncertainty on the term energies and each level's radiative lifetime, calculated using ExoCross (Yurchenko, Al-Refaie & Tennyson 2018), in keeping with the updated ExoMol format (Tennyson et al. 2023). While the updated ExoMol states file specification also includes the option of a column for Landé g-factors, these had not been implemented in the Duo hyperfine modules at the time of calculation. Were the Duo code updated to include this functionality, they could be computed using the hyperfine-resolved spectroscopic model for VO (Bowesman, Yurchenko & Tennyson 2023a) and added to the line list should the need arise to consider the effect of magnetic fields on the spectra of VO.

As has been used in other recent ExoMol line lists, a 'Source Tag' column is provided to indicate the method used to produce each final term value (Bowesman et al. 2021; McKemmish et al. 2024). The final line list consists of 28 760 MARVELized levels, labelled with 'Ma'; 105 566 levels energies adjusted have been based on obs.-calc. predicted shifts and are labelled 'PS'; 3276 272 levels are labelled 'Ca' and retain their energies as calculated by Duo. The number of MARVELized levels is greater than the number of MARVEL energies obtained by the earlier study (Bowesman et al. 2022), as the hyperfine-unresolved MARVEL energies were used for all hyperfine components of the hyperfine-unresolved electronic states. Using the same energy for each hyperfine component is valid here, given that according to experiment, the uncertainties in the hyperfine-unresolved MARVEL levels are set such that they are greater than the magnitude of their hyperfine splitting else they would have been resolved (Lagerqvist & Selin 1957; Cheung, Taylor & Merer 1982b; Merer et al. 1987; Cheung et al. 1994; Adam et al. 1995; Karlsson et al. 1997; Ram et al. 2002; Ram & Bernath 2005; Sriramachandran et al. 2008; Hopkins, Hamilton & Mackenzie 2009).

The trans files consist of a list of upper and lower state counting numbers, referencing the new states file, and an Einstein A coefficient giving the transition probability between the two states. Given the large number of transitions computed as part of the new line list, the trans files are provided as a series of archives each covering transitions within a 500 cm^{-1} range. An excerpt from one of the new trans files is given in Table 2.

The total number transitions calculated as part of the new line list is 58904 173243. The total number of MARVELized transitions, being the number of transitions with both upper and lower levels having MARVELized energies, is 1298 7450. This represents a very significant increase on the 8082 hyperfine-resolved and 9344 hyperfine-unresolved experimental transitions used to determine the MARVEL energies and serves as a strong example of the power the MARVEL technique has to predict new transitions frequencies with experimental accuracy. Also considering transitions between energy levels that have been adjusted with predicted shifts, the number of transitions that are known to a reasonably high accuracy increases to 9078 7509. An example of the distribution of the predicted shift energies amongst the MARVEL energies of the X $^4\Sigma^-$, $v = 1$ state can be seen in Fig. 2. Fig. 3 shows the contributions to the overall cross section from transitions between each possible combination of upper and lower level source tags, highlighting how the most intense transitions all involve at least one MARVELized or predicted shift energy level. Transitions between calculated levels provide the largest contribution at small cross sections, which is to be expected as levels involved in weaker transitions are less likely to be observed experimentally and hence not present in the MARVEL data set.

3.2 Partition functions

Partition functions for the new line list were calculated over a range of temperatures using the program ExoCross (Yurchenko, Al-Refaie & Tennyson 2018) and are shown in Table 3. The difference between these values and the partition function of the VOMYT line list (McKemmish, Yurchenko & Tennyson 2016b) increases with temperature and have separated by 5 per cent at approximately 5400 K. Though there are over five times as many levels in the new line list than in VOMYT (638 958 levels) the total degeneracies of the levels of VOMYT, which neglect hyperfine effects, are a factor of $g_{ns} = (2I + 1) = 8$ larger. Moreover, the VOMYT line list contains all states up to $J = 197.5$ with energies below 50 000 cm^{-1}, meaning approximately 216 619 levels (33.9 per cent of total) exist outside of the scope of the new line list. The number of levels is approximate as a J cut-off of 150.5 was taken for a comparison, whereas the new line list contains levels up to $F = 150$, meaning a small subset of levels with $J = 151.5$–153.5 are present. The contribution of these extra high-energy levels to the overall partition function will become more prominent at higher temperatures as their level population increases, accounting for most of the divergence between the two line lists. It is possible to calculate partition functions for the levels in VOMYT that are beyond the scope of the new line list and add them to the hyperfine-resolved partition functions to produce a more equivalent comparison. This is shown in Table 3, where the adjusted partition function is in much better agreement with the VOMYT line list. Indeed, this adjusted partition function never deviates from the VOMYT partition function by more than 1 per cent. Given the equivalence of the total degeneracies used in the line lists, this approximates the partition functions that would be obtained were the hyperfine-resolved model to be calculated up to $J = 197.5$.

Other partition functions for VO exist in the literature, often based on theoretical calculations with some adjustments owing to experiments but ultimately differing considerably from those of the new line list. For example, the partition functions of Sauval & Tatum (1984) are ∼35 per cent larger at 1000 K than they are for both the VOMYT and the new HyVO line lists, with the difference decreasing until reaching approximate agreement at 5000 K and falling off to ∼25 per cent smaller at 9000 K. Similarly, the partition functions of Barklem & Collet (2016) are slightly larger at low temperatures of $T < 100$ K, but fall off rapidly at higher temperatures to ∼40 per cent of the values presented in Table 3 at 5000 K and diverging further beyond that.

It can be noted that the first level to appear in the states file, shown in Table 1, with $F = 0$, does not have zero energy as it is not the zero-energy level. In the absence of hyperfine resolution, the lowest

Table 1. Excerpt from the $^{51}V^{16}O$ states file, using the format defined by Tennyson et al. (2013, 2023).

i	$\tilde{E}$	$g_{\rm tot}$	F	unc	τ	$+/-$	e/f	J	State	v	Λ	Σ	Ω	Source Tag	$\tilde{E}_{\rm calc}$
1	10.764111	1	0	0.002646	1.3052E+04	+	f	3.5	X(4SIGMA-)	0	0	0.5	0.5	Ma	10.773921
2	18.286612	1	0	0.002646	5.4524E+03	+	f	3.5	X(4SIGMA-)	0	0	1.5	1.5	Ma	18.329941
3	1012.490751	1	0	0.014945	5.2807E-02	+	f	3.5	X(4SIGMA-)	1	0	0.5	0.5	PS	1012.367510
4	1020.007393	1	0	0.001500	5.2805E-02	+	f	3.5	X(4SIGMA-)	1	0	1.5	1.5	Ma	1019.925017
5	2003.704567	1	0	0.009312	2.6738E-02	+	f	3.5	X(4SIGMA-)	2	0	0.5	0.5	PS	2003.948182
6	2011.289305	1	0	0.006908	2.6739E-02	+	f	3.5	X(4SIGMA-)	2	0	1.5	1.5	PS	2011.485588
7	2985.497918	1	0	0.280311	1.8054E-02	+	f	3.5	X(4SIGMA-)	3	0	0.5	0.5	Ca	2985.497918
8	2992.995747	1	0	0.280311	1.8056E-02	+	f	3.5	X(4SIGMA-)	3	0	1.5	1.5	Ca	2992.995747
9	3956.999417	1	0	0.330311	1.3718E-02	+	f	3.5	X(4SIGMA-)	4	0	0.5	0.5	Ca	3956.999417
10	3964.443764	1	0	0.330311	1.3720E-02	+	f	3.5	X(4SIGMA-)	4	0	1.5	1.5	Ca	3964.443764

Notes. i: State counting number;
$\tilde{E}$: Term value (in $\rm cm^{-1}$);
$g_{\rm tot}$: Total state degeneracy, $2F + 1$;
F: Final angular momentum, $F = J + I$;
unc: Estimated uncertainty of energy level (in $\rm cm^{-1}$);
τ: Radiative lifetime (in seconds);
$+/-$: Total parity;
e/f: Rotationless parity;
J: Total electron angular momentum;
State: Electronic state;
v: vibrational quantum number;
Λ: Projection of the electron orbital angular momentum;
Σ: Projection of the electron spin;
Ω: Projection of the total angular momentum, $\Omega = \Lambda + \Sigma$;
Source Tag: The method used to generate the term value; 'Ma' for MARVELized energies, 'PS' for energies from predicted shifts and, 'Ca' for energies calculated using DUO;
$\tilde{E}_{\rm calc}$: The original energy calculated by DUO.

Table 2. Excerpt from the $^{51}V^{16}O$ trans file, using the format defined by Tennyson, Hill & Yurchenko (2013). The below data come from the trans file detailing transitions between 0–500 $\rm cm^{-1}$.

f	i	A_{fi} ($\rm s^{-1}$)
328	6864	5.6380E-08
598	7659	5.7151E-07
975	8772	7.4097E-11
382	7023	2.9118E-18
166	6387	3.0935E-07
59	6069	1.3400E-37
490	7341	5.2938E-24
652	7818	1.0421E-12
1029	8931	7.0662E-13
219	6546	1.6189E-12

Note. f: the upper state counting number from the corresponding states file. *i*: the lower state counting number from the corresponding states file. A_{fi}: the Einstein A coefficient.

energy level in the system is the $J = 0.5$, e parity level in the F_1 fine structure component of the X $^4\Sigma^-$, $v = 0$ ground state. When hyperfine coupling is included, this level gives rise to two F levels with $F = 3$ and 4, of which $F = 3$ is lowest and hence the zero-energy level, i.e. taken to have energy zero in our line list.

3.3 ExoMolOP opacities

Molecular opacities of VO have been generated using the HyVO line list and following the ExoMolOP procedure (Chubb et al. 2021) for four exoplanet atmospheric retrieval codes ARCiS (Min et al. 2020), TauREx (Al-Refaie et al. 2021), NEMESIS (Irwin et al. 2008), and petitRADTRANS (Mollière et al. 2019). For the line broadening, we assumed an 85 per cent H_2 and 15 per cent He atmosphere and the

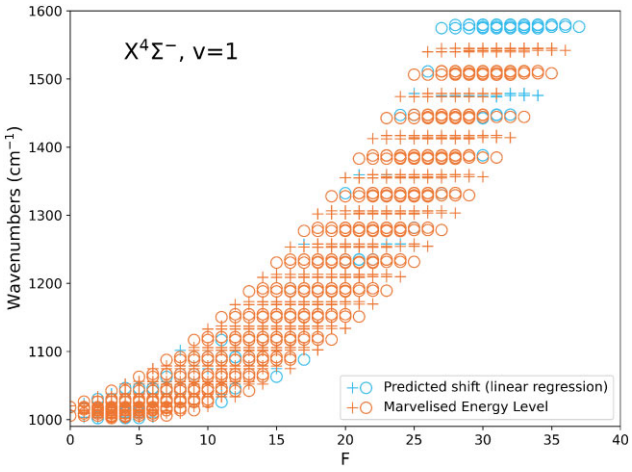

Figure 2. Combination of MARVELized and predicted shift energy levels in the X $^4\Sigma^-$, $v = 1$ state. Levels with positive total parity are marked with a '+' and those with negative total parity with 'o'.

Voigt line profile with the following parameters: $\gamma_{\rm H_2} = 0.19$ $\rm cm^{-1}$, $n_{\rm H_2} = 0.5$, $\gamma_{\rm He} = 0.10\,\rm cm^{-1}$, and $n_{\rm He} = 0.5$.

4 DISCUSSION

An example of the absorption spectrum generated from the new line list can be seen in Fig. 4, computed using the program EXOCROSS (Yurchenko, Al-Refaie & Tennyson 2018) for a variety of temperature up to 5000 K. This covers the main B $^4\Pi$–X $^4\Sigma^-$ and C $^4\Sigma^-$–X $^4\Sigma^-$ bands, which are expected to be the strongest features for observation in exoplanet atmospheres.

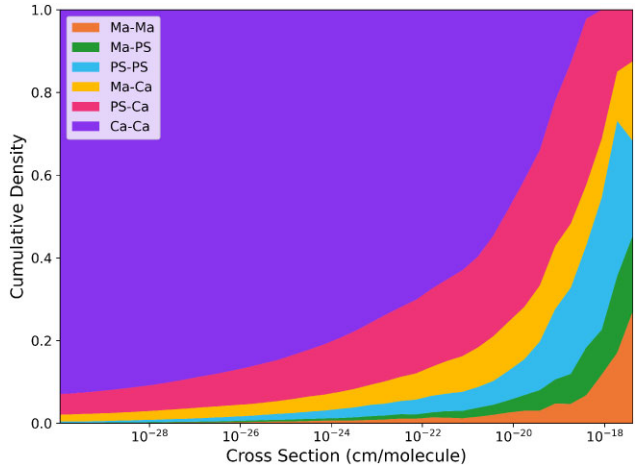

Figure 3. Probability density of transitions being between levels with each combination of source tags at a given intensity, in the spectrum of $^{51}V^{16}O$ at 2000 K computed using ExoCross (Yurchenko, Al-Refaie & Tennyson 2018). Transitions are grouped irrespective of which source tag belongs to the upper and lower energy level. 'Ma' denotes a MARVELized energy level; 'PS' denotes a predicted shift energy level and 'Ca' an energy calculated by Duo.

Table 3. Partition functions of $^{51}V^{16}O$ were calculated over a range of temperatures for the new line list presented here. The partition functions of the VOMYT line list are given as references, along with the contribution to the partition function from levels outside the scope of the new line list. An adjusted partition function for the new line list, with the added contribution from the VOMYT levels outside the quantum number and energy scope, is given for a more accurate comparison.

	Partition function			
Temp. (K)	HyVO	VOMYT	ΔPF	Adjusted
100	3.9097×10^{3}	3.9152×10^{3}	0.0000×10^{0}	3.9097×10^{3}
200	7.9850×10^{3}	7.9905×10^{3}	0.0000×10^{0}	7.9850×10^{3}
300	1.2154×10^{4}	1.2160×10^{4}	0.0000×10^{0}	1.2154×10^{4}
400	1.6588×10^{4}	1.6593×10^{4}	0.0000×10^{0}	1.6588×10^{4}
500	2.1423×10^{4}	2.1428×10^{4}	0.0000×10^{0}	2.1423×10^{4}
600	2.6740×10^{4}	2.6745×10^{4}	0.0000×10^{0}	2.6740×10^{4}
700	3.2581×10^{4}	3.2586×10^{4}	0.0000×10^{0}	3.2581×10^{4}
800	3.8971×10^{4}	3.8976×10^{4}	0.0000×10^{0}	3.8971×10^{4}
900	4.5926×10^{4}	4.5930×10^{4}	2.0000×10^{-4}	4.5926×10^{4}
1000	5.3460×10^{4}	5.3462×10^{4}	1.4000×10^{-3}	5.3460×10^{4}
1500	1.0037×10^{5}	1.0035×10^{5}	9.4060×10^{-1}	1.0037×10^{5}
2000	1.6556×10^{5}	1.6554×10^{5}	2.9106×10^{1}	1.6559×10^{5}
2500	2.5621×10^{5}	2.5642×10^{5}	2.6255×10^{2}	2.5647×10^{5}
3000	3.8289×10^{5}	3.8429×10^{5}	1.2726×10^{3}	3.8416×10^{5}
3500	5.5822×10^{5}	5.6325×10^{5}	4.2959×10^{3}	5.6251×10^{5}
4000	7.9548×10^{5}	8.0901×10^{5}	1.1469×10^{4}	8.0695×10^{5}
5000	1.5069×10^{6}	1.5670×10^{6}	5.2019×10^{4}	1.5589×10^{6}
6000	2.6073×10^{6}	2.7879×10^{6}	1.6032×10^{5}	2.7677×10^{6}
7000	4.1620×10^{6}	4.5870×10^{6}	3.8568×10^{5}	4.5476×10^{6}
8000	6.2072×10^{6}	7.0536×10^{6}	7.8170×10^{5}	6.9889×10^{6}
9000	8.7519×10^{6}	1.0245×10^{7}	1.3982×10^{6}	1.0150×10^{7}
10000	1.1782×10^{7}	1.4186×10^{7}	2.2754×10^{6}	1.4058×10^{7}

Given the lack of dipole moment curves for the 2 $^{2}\Delta$ and 3 $^{2}\Delta$ states in the new model, there are 51 dipole allowed electronic bands where $\Delta S = 0$, $\Delta\Lambda = 0, \pm 1$ (24 quartet-to-quartet and 27 doublet-to-doublet) though these selection rules are not rigorous, unlike the $\Delta F = 0, \pm 1$, and parity change selection rules. Consequently, a further 50 spin-forbidden bands between doublet and quartet states and 68 bands with $|\Delta\Lambda \geq 2|$ occur, facilitated through state mixing and intensity borrowing via spin-orbit coupling. Of these possible electronic bands, 99 different bands (32 dipole allowed, 31 spin forbidden, and 36 forbidden) provide contributions to the overall cross section on the order of 10^{-25} cm^2/molecule or larger at 2200 K. It can be seen in Fig. 5, however, which shows the individual electronic bands responsible for the main features in the spectrum of VO, that the spectrum is dominated by the A $^{4}\Pi$–X $^{4}\Sigma^{-}$, B $^{4}\Pi$–X $^{4}\Sigma^{-}$, and C $^{4}\Sigma^{-}$–X $^{4}\Sigma^{-}$ bands in the near-infrared and visible regions, in agreement with the bands reported in astronomical observations (Kirkpatrick et al. 1993; Kirkpatrick, Henry & Simons 1995; Kamiński, Schmidt & Tylenda 2010; Tylenda et al. 2011). Though some of the bands that are shown to provide large contributions to the overall cross section below 15 000 cm^{-1} seem to show an increase in their contributions at higher wavenumbers, this is most likely due to the mislabelling of states in higher vibrational bands as a result of state mixing. The primary feature from 30 000-45 000 cm^{-1} appears to be the forbidden D $^{4}\Delta$–X $^{4}\Sigma^{-}$ band, though state mixing at these higher energies means this is unclear.

While the strength of the C $^{4}\Sigma^{-}$–X $^{4}\Sigma^{-}$ band system decreases relative to the B $^{4}\Pi$–X $^{4}\Sigma^{-}$ system as temperature increases, it still remains the strongest component of VO spectra up to 5000 K, as seen in Fig. 4. Given that VO is believed to exist in hot Jupiter exoplanets across temperature ranges of approximately 1500–2800 K, consistent with its characterization of late M and early L dwarf spectra, the C $^{4}\Sigma^{-}$–X $^{4}\Sigma^{-}$ (0, 0) band head should be the single most prominent feature in its spectra. Due to the MARVELization procedure, this band is known to very high accuracy. The MARVELized transition frequencies across all vibrational bands of the C $^{4}\Sigma^{-}$–X $^{4}\Sigma^{-}$ system have a mean uncertainty of 0.0045 cm^{-1}, meaning the predicted line positions are accurate to a mean instrumental resolving power of approximately $\bar{R} = 4\,000\,000$. Above this resolving power, deviations in the line positions arising from the limits on the uncertainties in the MARVEL energy levels would be resolvable. Similarly, the MARVELized B $^{4}\Pi$–X $^{4}\Sigma^{-}$ transition frequencies have a mean uncertainty of 0.0041 cm^{-1}, which given their position in the infrared corresponds to an accuracy up to a resolving power of $\bar{R} = 3000\,000$.

For other important electronic bands where one or more electronic state is not hyperfine resolved, the uncertainty in the line positions are larger but still well suited for high-resolution studies. This includes the strong A $^{4}\Pi$–X $^{4}\Sigma^{-}$ band with a mean uncertainty in the transition frequencies of 0.064 cm^{-1}, hence accurate up to resolving powers of $\bar{R} = 140\,000$. Some of the other important features in the spectrum of VO, such as the B $^{4}\Pi$–A $^{4}\Pi$ system with its prominent peak around 3000 cm^{-1} and the 1 $^{2}\Phi$–1 $^{2}\Delta$ system with its contributions to the peaks from 3500–6500 cm^{-1} shown in Fig. 5, have larger mean uncertainties in their transition frequencies: 0.064 and 0.31 cm^{-1}, respectively. This means the new line list has comparatively limited accuracy for these bands, with deviations from the predicted line positions becoming resolvable at resolving powers of $\bar{R} = 49\,000$ and 17 000. This is owing to the lower accuracy of the empirical MARVEL energies derived from hyperfine-unresolved transition data. Indeed, some of the experimental data for the 1 $^{2}\Phi$ state was not of sufficiently high-resolution to resolve parity splitting, so the derived MARVEL energies are less accurate.

Given the MARVEL data only includes transitions with full quantum number assignments, the vibrational coverage of most electronic states is somewhat limited. To combat this, the model of Bowesman, Yurchenko & Tennyson (2023a) was also fit to the band heads of higher vibrational bands where available: Hopkins, Hamilton & Mackenzie (2009) provided effective Hamiltonian constants to calcu-

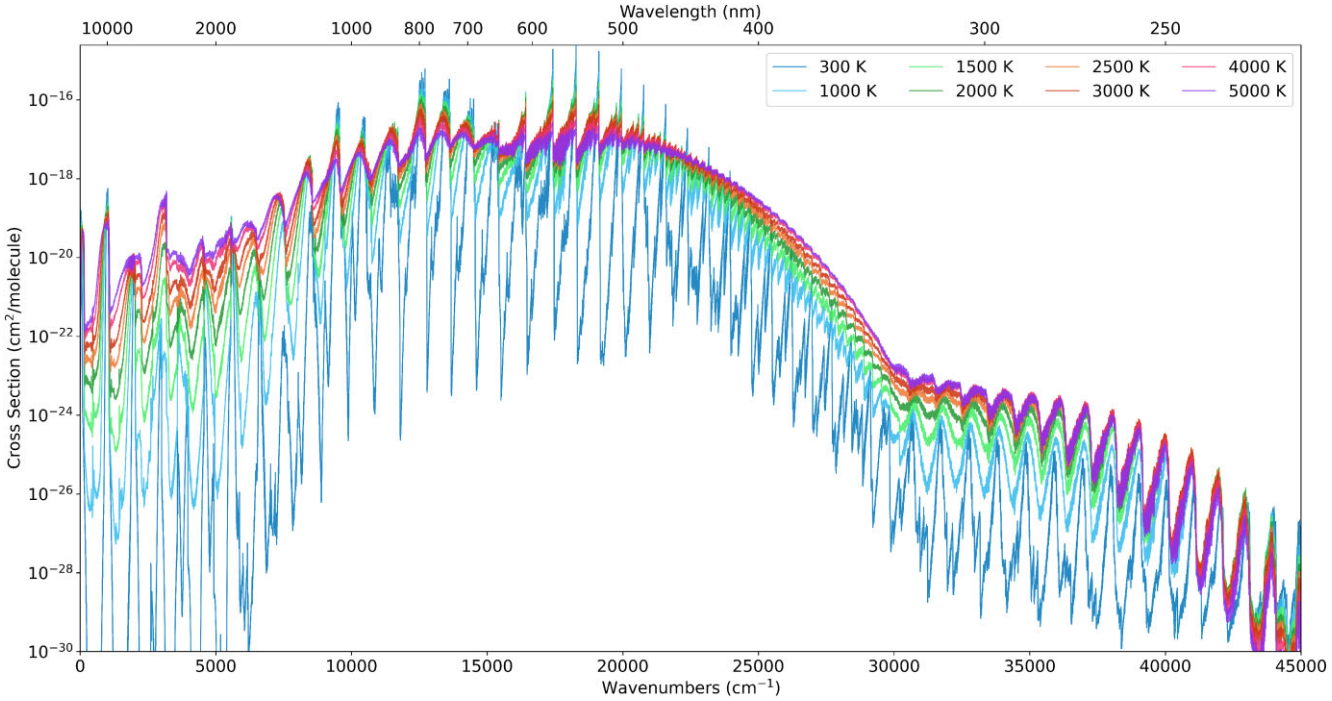

Figure 4. Absorption spectra of $^{51}V^{16}O$ at a variety of temperatures up to 5000 K, computed using the program ExoCross (Yurchenko, Al-Refaie & Tennyson 2018) between 0-45 000 cm^{-1}. These spectra were computed using Gaussian line profiles with a half width at half-maximum of 0.2 cm^{-1}.

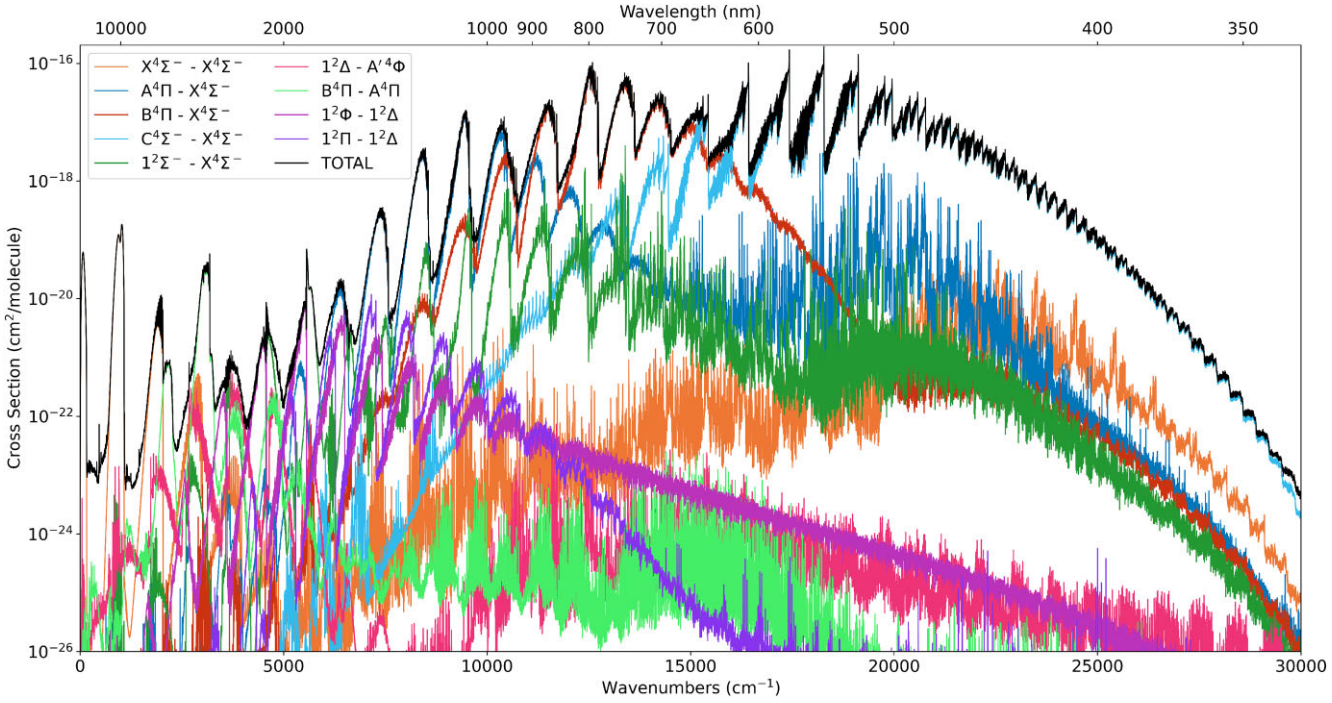

Figure 5. Decomposition of the absorption spectrum of $^{51}V^{16}O$ at 2200 K was computed using the program ExoCross (Yurchenko, Al-Refaie & Tennyson 2018), between 0–30 000 cm^{-1}. The individual contributions to the overall spectrum from several of the strongest electronic bands that contribute to the majority of the most prominent features are shown. The spectrum was computed using Gaussian line profiles with a half width at half-maximum of 1 cm^{-1}.

late vibrational band origins for the B $^4\Pi v = 4$, C $^4\Sigma^- v = 3$–6, and 2 $^2\Pi v = 4$ states; Mahanti (1935) provided band head measurements for transitions involving the X $^4\Sigma^- v = 3$–8 and C $^4\Sigma^- v = 7$–8 states. Hence, the predicted band origins for features arising from these states should also be reliable.

4.1 Hyperfine effects

Though the number of energy levels is increased by approximately a factor of 8 under hyperfine coupling, due to the splitting of each J into F values in the range $|J - I| \leq F \leq J + I$, the increase

in the number of transitions is much greater – approximately 64. This is a result of how the hyperfine coupling $F = J + I$ allows for transitions forbidden under the dipole selection rule $\Delta J = 0, \pm 1$ to occur, as the selection rule transforms to $\Delta F = 0, \pm 1$. Consequently, transitions up to $|\Delta J| = 8$ are allowed. Despite this, it has been shown in earlier work on the hyperfine-resolved ground state of VO by Qu, Yurchenko & Tennyson (2022b) that Einstein A coefficients and hence intensities decrease rapidly above $|\Delta J| = 3$. Experimental measurements have only been reported up to $|\Delta J| = 2$, however (Cheung, Hansen & Merer 1982a; Cheung et al. 1994; Adam et al. 1995; Karlsson et al. 1997). Though propensity rules favour transitions with $\Delta F = \Delta J$, those where $\Delta F \neq \Delta J$ do occur (Cheung, Hansen & Merer 1982a; Suenram et al. 1991; Adam et al. 1995; Flory & Ziurys 2008; Döring et al. 2022) and are referred to as hyperfine satellites. It can be seen in Fig. 6 that as the difference between ΔF and ΔJ becomes larger, transitions get weaker. Given that the new line list comprises just under 59 billion transitions, modifications were made to the hyperfine modules of the Duo code (Qu, Yurchenko & Tennyson 2022a) to parallelize the computation of Einstein A coefficients, in order to significantly reduce the computation time.

Considering how the new line list compares to hyperfine-unresolved transitions, what would have previously been considered a single $\Delta J = 0$ Q-branch transition now exists as 22 hyperfine transitions – 8 transitions with $\Delta F = 0$ and 7 each for $\Delta F = \pm 1$. While the number of hyperfine transitions decreases as $|\Delta J|$ increases, down to 1 for $|\Delta J| = 8$, the single feature you would expect to see in a hyperfine-unresolved spectrum becomes spread out due to hyperfine coupling. An example of the 21 components comprising a standard R-branch transitions are shown in Fig. 6. It should be noted that the difference in the cross sections of the hyperfine transitions of the new line list compared to those of VOMYT are due to changes in the underlying potential energy, coupling and transition dipole moment curves of the spectroscopic model and not simply due to the introduction of hyperfine couplings. The total integrated cross section of a given transition is conserved upon the introduction of hyperfine couplings and the splitting of the transitions into its hyperfine components. In the known experimental data for the C $^4\Sigma^-$–X $^4\Sigma^-$ and B $^4\Pi$–X $^4\Sigma^-$ systems, the hyperfine components of what would be considered a single transition in the absence of hyperfine couplings have a median spread over 0.198 and 0.188 cm^{-1}, respectively. For both systems, approximately 45 per cent of experimental transitions have hyperfine splitting between 0.2–0.4 cm^{-1}, with a tail off up to $\sim$0.6 cm^{-1}. An example of rotational transitions with hyperfine components spread over this range can be seen in Fig. 7. Consequently, and given the positions of these band systems, these hyperfine splittings will start to be resolvable at resolving powers of $R \approx 30\,000$. While at temperatures such as 2200 K, the Doppler-broadened line profiles of these bands will have half width at half-maximum (HWHM) values of $\approx$0.025–0.035 cm^{-1}, Fig. 7 shows how multiple rotational bands overlap and individual hyperfine transitions are significantly blended. Consequently, the convolution of individual line profiles is decidedly non-Gaussian and the overall cross section differs greatly from that of the spectrum without hyperfine effects (Qu, Yurchenko & Tennyson 2022b). Given high-resolution cross-correlation studies aim for a resolving power of $R = 100\,000$ for a reliable detection, the inclusion of hyperfine effects is hence necessary for a line list to be used with such high-resolution techniques. Moreover, it is possible that failure to consider hyperfine effects in the spectra of $^{51}V^{16}O$, with their impact on the overall cross section and broadening of spectral features, may lead to the mischaracterization of the thermal broadening present in exoplanet spectra. This could in turn lead to the improper determination of physical properties such as atmospheric temperature during an exoplanet retrieval. Though many of the resolving powers discussed here are much greater than the capabilities of the instruments onboard the JWST, with $R \approx 3000$, the adjusted intensities presented here will also result in a change in the derived atmospheric abundances at any resolution.

4.2 VOMYT comparisons

Individual transitions in the new line list appear quite differently to those in the VOMYT line list, not just because of the splitting of transitions into multiple hyperfine components, but also due to the redistribution of intensities. As shown in Fig. 6, while the hyperfine transitions are spread across $\approx$0.2 cm^{-1} either side of the equivalent C $^4\Sigma^-$–X $^4\Sigma^-$ (0,0) $R_1(J = 4.5)$ transition from VOMYT, which neglects hyperfine effects, they are also significantly more intense. The C $^4\Sigma^-$–X $^4\Sigma^-$ (0, 0) band overall is only slightly stronger in the new line list, but the intensities of individual transitions have been redistributed, as can be seen in Fig. 7. This is not surprising given the refitting of the electronic state potentials and couplings (Bowesman, Yurchenko & Tennyson 2023a). In particular, considerable adjustments were made to the off-diagonal spin-orbit couplings in the model that are principally responsible for the intensity of borrowing between electronic states.

While the $(v', v'') = (0, 0)$ bands in the VOMYT model generally most accurately recreated experimental band head measurements, the new model is much better at reproducing the higher vibrational bands for which experimental data was available. Fig. 8 shows an example of the C $^4\Sigma^-$–X $^4\Sigma^-$ (2, 0) band, one of the strongest features in the spectrum of VO, which has shifted by several wavenumbers as a result of the refitting of the C $^4\Sigma^-$ state. Even in low resolution experiments that are not able to resolve the hyperfine structure, this change in position, intensity, and shape will be noticeable, highlighting how the new line list is better suited for experiments at all resolutions. It should be noted that an earlier work (Bowesman et al. 2022) misidentified a band feature at 18 952 cm^{-1} as the C $^4\Sigma^-$–X $^4\Sigma^-$ (2, 0) band, though it was actually the (3, 1) band. This mislabelling was not used in the construction of the MARVEL network or spectroscopic model and does not impact the accuracy of the new line list.

Table 4 gives the mean lifetimes for the levels in each spin-orbit or fine structure component of each vibronic state in the new line list and in VOMYT. As discussed in Section 2.1, the three dipole moment curves between the A $^4\Pi$, B $^4\Pi$, and C $^4\Sigma^-$ states and the ground state were scaled to bring the final vibronic lifetimes in line with the experimental values obtained by Karlsson et al. (1997). This dipole scaling is the primary cause of the difference in the lifetimes of these three states between the HyVO and VOMYT line lists and will have knock-on effects for other state lifetimes as a result of intensity borrowing through spin-orbit coupling.

The lifetimes of states with $v = 0$ in the new line list are on average almost 12 times smaller than they were in VOMYT, but this is skewed by several states. The 1 $^2\Pi$ and 2 $^2\Pi$, $v = 0$ states have lifetimes over ten times smaller in the new line list, likely because the VOMYT model did not include spin-orbit coupling to the C $^4\Sigma^-$ state, which provided a mechanism for the intensity stealing that facilitates the spin-forbidden 2 $^2\Pi$–X $^4\Sigma^-$ band observed by

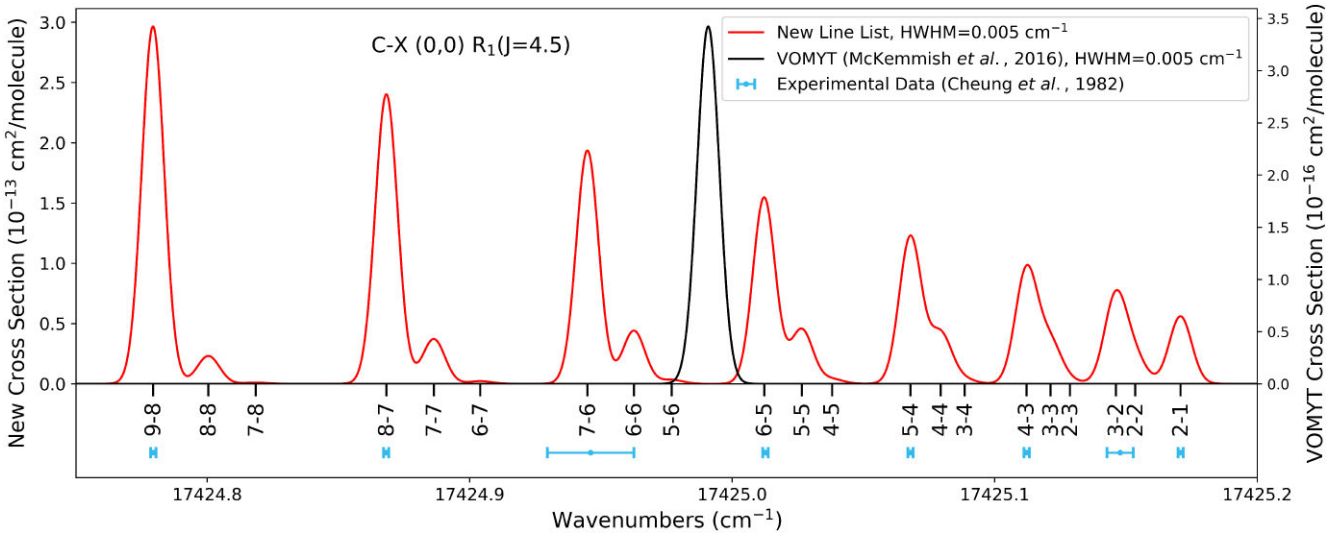

Figure 6. $C\,^4\Sigma^- – X\,^4\Sigma^-$ (0, 0) $R_1(J = 4.5)$ transitions in the absorption spectrum of $^{51}V^{16}O$ computed using the program ExoCross (Yurchenko, Al-Refaie & Tennyson 2018) at 2200 K. The spectra were generated using Gaussian line profiles with HWHM of 0.005 cm^{-1} and are marked with their $F' \leftarrow F''$ values. Note that the new, hyperfinely resolved spectrum in red uses the left-hand axis, and the VOMYT spectra in black use the right-hand axis. Transitions with $\Delta F = +1$ are the strongest, as is expected for $\Delta J = +1$ transition with $\Delta F = 0$ transitions being weaker but still noticeable, and those with $\Delta F = -1$ being heavily blended and difficult to distinguish. This coincides with the experimental observations for these transitions recorded by Cheung, Hansen & Merer (1982a), shown in blue in the bottom panel, who only observed $\Delta F = +1$ transitions. The higher uncertainty in the $7 \leftarrow 6$ transition was due to severe blending leading to an initial misassignment to the $6 \leftarrow 6$ transition.

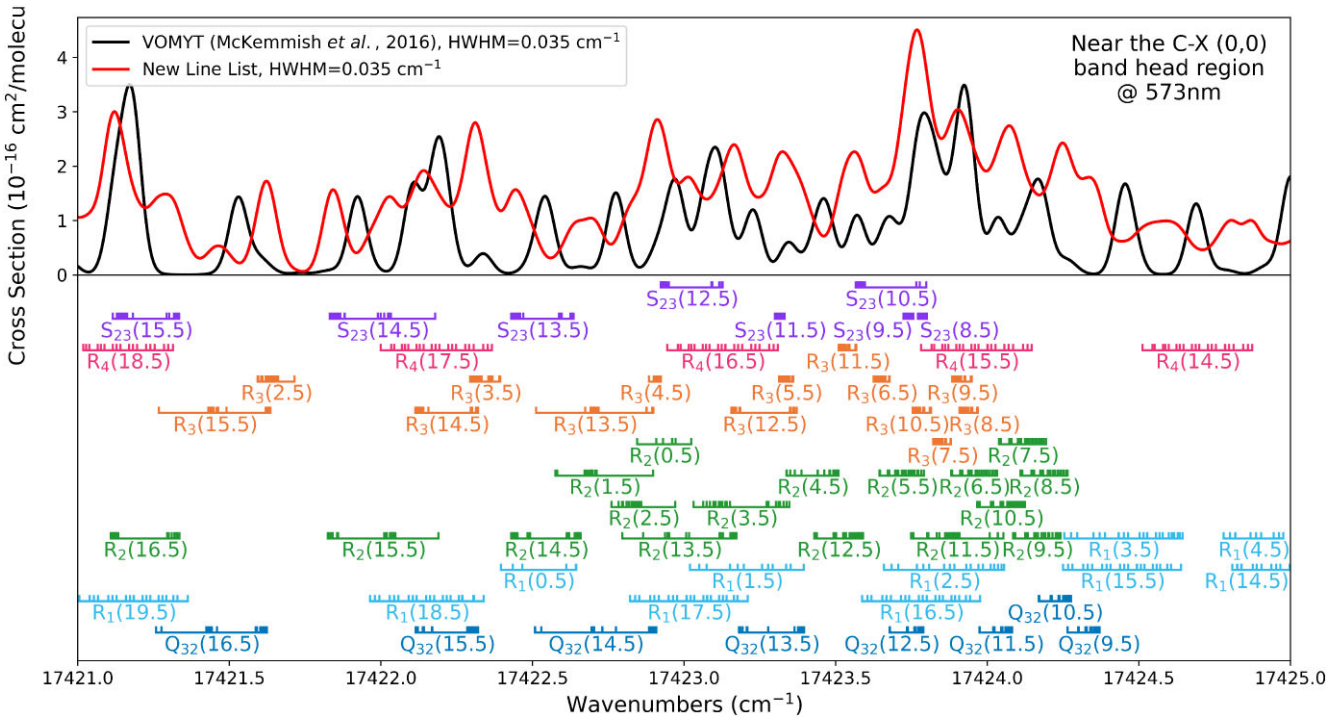

Figure 7. Close-up near the $C\,^4\Sigma^- – X\,^4\Sigma^-$ (0, 0) band head in the absorption spectra of $^{51}V^{16}O$, computed using the program ExoCross (Yurchenko, Al-Refaie & Tennyson 2018) at 2200 K. The spectra were generated using Gaussian line profiles with HWHM of 0.035 cm^{-1} to demonstrate that the complicated arrangement of line positions and their individual intensities are very different in the new line list compared to that of the older VOMYT line list (McKemmish, Yurchenko & Tennyson 2016b). Rotational assignments to the strongest transitions in this region are marked in the bottom panel, with the number in brackets being the lower state J assignment. Stick marks are used to identify each hyperfine component of a rotational transition: the 63 rotational transitions shown here comprise 1250 hyperfine components. The new line list contains a total of 1309 241 hyperfine transitions in the 4 cm^{-1} range shown in this plot.

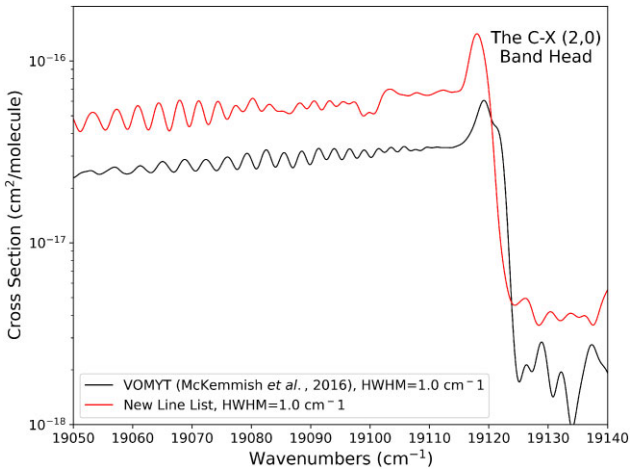

Figure 8. C $^4\Sigma^-$–X $^4\Sigma^-$ (2, 0) band head in the absorption spectra of $^{51}V^{16}O$, computed using the program ExoCross (Yurchenko, Al-Refaie & Tennyson 2018) at 2200 K. The spectra were generated using Gaussian line profiles with HWHM of 1.0 cm^{-1}, showing an example of how many entire bands are shifted compared to the VOMYT line list (McKemmish, Yurchenko & Tennyson 2016b) at resolutions relevant to high-resolution studies.

Hopkins, Hamilton & Mackenzie (2009). The 1 $^2\Phi$, $v = 0$ lifetimes are now almost 70 times smaller, however, and are likely due to a combination of its refit electronic state potential and spin-orbit interactions and the correction to the transition dipole moments affecting states with $\Lambda \geq 1$ mentioned in Section 2.1. This is also likely the cause of the factor of 10 reduction in the 1 $^2\Gamma$ and factor of 25 reduction in the $1^2\Sigma^-$, $v = 0$ lifetimes.

5 CONCLUSIONS

A new, high-resolution line list for $^{51}V^{16}O$ has been produced, intended to replace the existing ExoMol line list (McKemmish, Yurchenko & Tennyson 2016b). The new line list is based on the hyperfine-resolved spectroscopic model of Bowesman, Yurchenko & Tennyson (2023a) and is computed using the program Duo (Yurchenko et al. 2016) with its recently added hyperfine coupling modules (Qu, Yurchenko & Tennyson 2022a). Based on earlier *ab initio* (McKemmish, Yurchenko & Tennyson 2016a; Qu, Yurchenko & Tennyson 2022b) and empirical (Qu, Yurchenko & Tennyson 2023) studies, this model was refined against empirical term energies derived from the MARVEL procedure (Bowesman et al. 2022) to enable the accurate recreation of experimental transition measurements. Accordingly, this new line list should enable the more reliable high-resolution detection of the molecule in both stellar and exoplanet atmospheres, which the previous line list was unable to facilitate due to the absence of hyperfine effects (de Regt et al. 2022).

Sriramachandran et al. (2008) identified four vibrational bands of the C $^4\Sigma^-$–X $^4\Sigma^-$ system in sunspot spectra. While their measurements were incorporated into the MARVEL network (Bowesman et al. 2022), they were only able to identify a limited number of rotational transitions. The new line list provides high-accuracy predictions for transitions in these bands and could be used in conjunction with high-resolution spectra to assign additional sunspot features.

While the levels of the X $^4\Sigma^-$, B $^4\Pi$, and C $^4\Sigma^-$ states are fully hyperfine-resolved, levels from other electronic states use hyperfine-unresolved term energies for all of their hyperfine components due to limited experimental resolution. As such, hyperfine-resolved spectroscopic studies of important bands such as the A $^4\Pi$–X $^4\Sigma^-$ system would enable the further improvement of the line list by characterizing the currently poorly quantified hyperfine splitting in the A $^4\Pi$ state. If studies aim to observe VO further into the UV, calculations could be performed for transition dipole moments involving the 2 $^2\Delta$ and 3 $^2\Delta$ states to better characterize their contributions to the spectra in these regions. A proper treatment of these two states would require the addition of nine transition dipole moments and 16 off-diagonal spin-orbit couplings to the current model, which, given the high degree of correlation between the model parameters, would likely require extensive refinement.

The roughly 59 billion transitions in the new line list are a considerable increase on the 277 million transitions that made up the VOMYT line list. Owing to the significant increase in energy levels as a result of hyperfine coupling, the number of transitions in the new line list is closer to line lists of polyatomic molecules than it is for other diatomics. With the current implementation of Duo, the spectroscopic model calculations required a significant amount of computer resources and made use of the DiRAC Data Intensive service at the Leicester high-performance cluster. While the VO line list could be extended to consider some of the additional known electronically excited states, particularly those lying at higher

Table 4. Mean radiative lifetimes in the first two vibrational bands of each state, compared against the VOMYT line list and experimental measurements of Karlsson et al. (1997). The lowest energy levels in the X $^4\Sigma^-$ state with infinite lifetimes were excluded from the calculations. The mean lifetimes of the VOMYT line list were calculated over levels with $J \leq 150.5$ for a more equivalent comparison to the $F \leq 150$ of the new HyVO line list.

	$v = 0$ mean lifetime (s)			$v = 1$ mean lifetime (s)		
State	HyVO	VOMYT	Experiment	HyVO	VOMYT	Experiment
X $^4\Sigma^-$	5.19×10^{4}	1.03×10^{5}	–	5.34×10^{-2}	5.32×10^{-2}	–
1 $^2\Sigma^-$	6.51×10^{-3}	1.69×10^{-1}	–	4.71×10^{-3}	7.49×10^{-2}	–
A′ $^4\Phi$	9.61×10^{1}	7.63×10^{1}	–	9.16×10^{-2}	8.98×10^{-2}	–
1 $^2\Gamma$	3.43×10^{0}	3.66×10^{1}	–	7.07×10^{-2}	7.41×10^{-2}	–
A $^4\Pi$	5.82×10^{-6}	2.29×10^{-5}	5.8×10^{-6}	5.88×10^{-6}	2.34×10^{-5}	–
1 $^2\Delta$	5.15×10^{-4}	2.78×10^{-3}	–	1.60×10^{-3}	5.53×10^{-3}	–
1 $^2\Sigma^+$	1.48×10^{-4}	1.89×10^{-4}	–	1.68×10^{-4}	2.71×10^{-4}	–
B $^4\Pi$	4.03×10^{-7}	9.94×10^{-7}	3.74×10^{-7}	3.86×10^{-7}	9.71×10^{-7}	4.07×10^{-7}
1 $^2\Phi$	2.88×10^{-5}	1.97×10^{-3}	–	2.60×10^{-5}	9.82×10^{-5}	–
1 $^2\Pi$	9.19×10^{-6}	1.18×10^{-4}	–	9.40×10^{-6}	6.25×10^{-5}	–
C $^4\Sigma^-$	6.88×10^{-8}	1.18×10^{-7}	7.3×10^{-8}	6.80×10^{-8}	1.16×10^{-7}	6.3×10^{-8}
2 $^2\Pi$	1.03×10^{-5}	1.53×10^{-4}	–	1.03×10^{-5}	1.21×10^{-4}	–
D $^4\Delta$	1.22×10^{-5}	2.70×10^{-5}	–	1.09×10^{-5}	2.45×10^{-5}	–

energies, the calculations using our spectroscopic model would rapidly approach the limits of the computer resources available to us. Accordingly, it would first be necessary to optimize or restructure parts of the code before tackling larger and more complex systems.

ACKNOWLEDGEMENTS

This work was supported by the European Research Council (ERC) under the European Union's Horizon 2020 research and innovation programme through Advance Grant number 883830 and the UK STFC under grant ST/R000476/1. The DUO calculations of this work were performed using the DiRAC Data Intensive service at Leicester, operated by the University of Leicester IT Services, which forms part of the STFC DiRAC HPC Facility (https://dirac.ac.uk). The equipment was funded by BEIS capital funding via STFC capital grants ST/K000373/1 and ST/R002363/1 and STFC DiRAC Operations grant ST/R001014/1. DiRAC is part of the National e-Infrastructure.

DATA AVAILABILITY

The DUO input file used to compute the new line list and the MARVEL energy levels used for MARVELizing and predicting shifts in the model are given as supporting material. The DUO code is made available at https://github.com/Trovemaster/Duo. The new HyVO line list is available via the https://exomol.com website.

REFERENCES

Adam A. G., Barnes M., Berno B., Bower R. D., Merer A. J., 1995, J. Mol. Spectrosc., 170, 94
Al-Derzi A. R. et al., 2021, J. Quant. Spectrosc. Radiat. Transf., 266, 107563
Al-Refaie A. F., Changeat Q., Waldmann I. P., Tinetti G., 2021, ApJ, 917, 37
Ali-Dib M., Mousis O., Pekmezci G. S., Lunine J. I., Madhusudhan N., Petit J.-M., 2014, A&A, 561, A60
Barklem P. S., Collet R., 2016, A&A, 588, A96
Ben-Yami M., Madhusudhan N., Cabot S. H. C., Constantinou S., Piette A., Gandhi S., Welbanks L., 2020, ApJL, 897, L5
Bowesman C. A., Shuai M., Yurchenko S. N., Tennyson J., 2021, MNRAS, 508, 3181
Bowesman C. A., Akbari H., Hopkins S., Yurchenko S. N., Tennyson J., 2022, J. Quant. Spectrosc. Radiat. Transf., 289, 108295
Bowesman C. A., Yurchenko S. N., Tennyson J., 2023a, Mol. Phys., e2255299
Bowesman C. A. et al., 2023b, MNRAS, 519, 6333
Castelaz M. W., Luttermoser D. G., Piontek R. A., 2000, ApJ, 538, 341
Cheung A. S. C., Hansen R. C., Merer A. J., 1982a, J. Mol. Spectrosc., 91, 165
Cheung A. S. C., Taylor A. W., Merer A. J., 1982b, J. Mol. Spectrosc., 92, 391
Cheung A. S. C., Hajigeorgiou P. G., Huang G., Huang S. Z., Merer A. J., 1994, J. Mol. Spectrosc., 163, 443
Chubb K. L. et al., 2021, A&A, 646, A21
Coulombe L.-P. et al., 2023, Nature, 620, 292
Cushing M. C., Rayner J. T., Vacca W. D., 2005, ApJ, 623, 1115
de Regt S., Kesseli A. Y., Snellen I. A. G., Merritt S. R., Chubb K. L., 2022, A&A, 661, A109
Désert J.-M., Vidal-Madjar A., Lecavelier des Etangs A., Sing D., Ehrenreich D., Hébrard G., Ferlet R., 2008, A&A, 492, 585
Dinh-V-Trung Bao N. T. T., Tien P. M., Hai B. V., Minh P. H., Khiem L. H., 2022, AJ., 164, 219
Döring E., Fuchs G. W., Giesen T., Breier A. A., Blum L., 2022, in 2022 International Symposium on Molecular Spectroscopy. University of Illinois, Urbana-Champaign, Il, USA, p. FG11
Evans T. M. et al., 2016, ApJ, 822, L4
Evans T. M. et al., 2018, AJ., 156, 283
Fawley W. M., 1977, ApJ, 218, 181
Flory M. A., Ziurys L. M., 2008, J. Mol. Spectrosc., 247, 76
Fortney J. J., Lodders K., Marley M. S., Freedman R. S., 2008, ApJ, 678, 1419
Gandhi S., Madhusudhan N., 2019, MNRAS, 485, 5817
Goranskii V. P., Barsukova E. A., 2007, Astron. Rep., 51, 126
Goyal J. M. et al., 2020, MNRAS, 498, 4680
Haynes K., Mandell A. M., Madhusudhan N., Deming D., Knutson H., 2015, ApJ, 806, 146
Hillenbrand L. A., Knapp G. R., Padgett D. L., Rebull L. M., McGehee P. M., 2012, AJ., 143, 37
Hocking W. H., Merer A. J., Milton D. J., 1981, Can. J. Phys., 59, 266
Hoeijmakers H. J. et al., 2020, A&A, 641, A123
Hopkins W. S., Hamilton S. M., Mackenzie S. R., 2009, J. Chem. Phys., 130, 144308
Hubeny I., Burrows A., Sudarsky D., 2003, ApJ, 594, 1011
Huber P. J., Ronchetti E. M., 2009, Robust Statistics, Second Edition. Wiley, Hoboken, NJ, USA
Hübner O., Hornung J., Himmel H.-J., 2015, J. Chem. Phys., 143, 024309
Humphreys R. M. et al., 2019, ApJL, 874, L26
Irwin P. G. J. et al., 2008, J. Quant. Spectrosc. Radiat. Transf., 109, 1136
Johnson M. C. et al., 2023, AJ., 165, 157
Kamiński T., Schmidt M., Tylenda R., Konacki M., Gromadzki M., 2009, ApJS, 182, 33
Kamiński T., Schmidt M., Tylenda R., 2010, A&A, 522, A75
Karlsson L., Lindgren B., Lundevall C., Sassenberg U., 1997, J. Mol. Spectrosc., 181, 274
Keenan P. C., Schroeder L. W., 1952, ApJ, 115, 82
Kirkpatrick J. D., Henry T. J., McCarthy D. W., Jr, 1991, ApJS, 77, 417
Kirkpatrick J. D., Kelly D. M., Rieke G. H., Liebert J., Allard F., Wehrse R., 1993, ApJ, 402, 643
Kirkpatrick J. D., Henry T. J., Simons D. A., 1995, AJ., 109, 797
Lagerqvist A., Selin L. E., 1957, Ark. Fys., 11, 429
Lançon A., Hauschildt P. H., Ladjal D., Mouhcine M., 2007, A&A, 468, 205
Liimets T. et al., 2022, A&A, 670, A13
Lockwood G. W., Wing R. F., 1982, MNRAS, 198, 385
Loebman S. R. et al., 2014, AJ., 149, 17
Lothringer J. D., Barman T., Koskinen T., 2018, ApJ, 866, 27
Mahanti P. C., 1935, Proc. Phys. Soc., 47, 433
McKemmish L. K., Yurchenko S. N., Tennyson J., 2016a, Mol. Phys., 114, 3232
McKemmish L. K., Yurchenko S. N., Tennyson J., 2016b, MNRAS, 463, 771
McKemmish L. K., Masseron T., Hoeijmakers J., Pérez-Mesa V. V., Grimm S. L., Yurchenko S. N., Tennyson J., 2019, MNRAS, 488, 2836
McKemmish L. K., Syme A. M., Bowesman C. A., Kefela K., Yurchenko S. N., Tennyson J., 2024, RASTI (in preparation)
Mellor T., Owens A., Yurchenko S. N., Tennyson J., 2022, MNRAS, 520, 1997
Merer A. J., Huang G., Cheung A. S. C., Taylor A. W., 1987, J. Mol. Spectrosc., 125, 465
Merrill P. W., Deutsch A. J., Keenan P. C., 1962, ApJ, 136, 21
Merritt S. R. et al., 2020, A&A, 636, A117
Merritt S. R. et al., 2021, MNRAS, 506, 3853
Min M., Ormel C. W., Chubb K., Helling C., Kawashima Y., 2020, A&A, 642, A28
Mollière P., Wardenier J. P., van Boekel R., Henning T., Molaverdikhani K., Snellen I. A. G., 2019, A&A, 627, A67
Owen A. B., 2007, in Contemp. Math., Vol. 443, Prediction and discovery. Amer. Math. Soc., Providence, RI, p. 59
Owens A., Dooley S., McLaughlin L., Tan B., Zhang G., Yurchenko S. N., Tennyson J., 2022a, MNRAS, 511, 5448
Owens A., Mitrushchenkov A., Yurchenko S. N., Tennyson J., 2022b, MNRAS, 516, 3995
Pavlenko Y. V., Yurchenko S. N., McKemmish L. K., Tennyson J., 2020, A&A, 42, A77
Pedregosa F. et al., 2011, J. Mach. Learn. Res., 12, 2825
Pelletier S. et al., 2023, Nature, 619, 491
Prinoth B. et al., 2022, Nat. Astron., 6, 449
Qu Q., Yurchenko S. N., Tennyson J., 2022a, J. Chem. Theory Comput., 18, 1808

Qu Q., Yurchenko S. N., Tennyson J., 2022b, J. Chem. Phys., 157, 124305
Qu Q., Yurchenko S. N., Tennyson J., 2023, J. Mol. Spectrosc., 391, 111733
Rajpurohit A.-S., Reylé C., Schultheis M., Allard F., Scholz R., Homeier D., 2012, in Boissier S., de Laverny P., Nardetto N., Samadi R., Valls-Gabaud D., Wozniak H., eds, SF2A-2012: Proceedings of the Annual meeting of the French Society of Astronomy and Astrophysics. Société Française d'Astronomie et d'Astrophysique, France, p. 383, https://ui.adsabs.harvard.edu/abs/2012sf2a.conf..383R
Rajpurohit A. S., Reylé C., Allard F., Scholz R. D., Homeier D., Schultheis M., Bayo A., 2014, A&A, 564, A90
Ram R. S., Bernath P. F., 2005, J. Mol. Spectrosc., 229, 57
Ram R. S., Bernath P. F., Davis S. P., Merer A. J., 2002, J. Mol. Spectrosc., 211, 279
Sauval A. J., Tatum J. B., 1984, ApJS, 56, 193
Schwarz H., Brogi M., de Kok R., Birkby J., Snellen I., 2015, A&A, 576, A111
Semenov M., Tennyson J., Yurchenko S. N., 2022, Phys. Chem. Chem. Phys., 516, 1158
Sharp C. M., Burrows A., 2007, ApJS, 168, 140
Showman A. P., Fortney J. J., Lian Y., Marley M. S., Freedman R. S., Knutson H. A., Charbonneau D., 2009, ApJ, 699, 564
Simeckova M., Jacquemart D., Rothman L. S., Gamache R. R., Goldman A., 2006, J. Quant. Spectrosc. Radiat. Transf., 98, 130
Spiegel D. S., Silverio K., Burrows A., 2009, ApJ, 699, 1487
Spinrad H., Wing R. F., 1969, ARA&A, 7, 249
Spinrad H., Younkin R. L., 1966, PASP, 78, 65
Sriramachandran P., Bagare S. P., Rajamanickam N., Balachandrakumar K., 2008, Sol. Phys., 252, 267
Stone N., 2005, At. Data Nucl. Data Tables, 90, 75
Suenram R. D., Fraser G. T., Lovas F. J., Gillies C. W., 1991, J. Mol. Spectrosc., 148, 114
Tennyson J., Hill C., Yurchenko S. N., 2013, AIP Conf. Proc. Vol. 1545, 6th international conference on atomic and molecular data and their applications ICAMDATA-2012, Am. Inst. Phys., New York, p. 186
Tennyson J., Pezzella M., Zhang J., Yurchenko S. N., 2023, RASTI, 2, 231
Tsiaras A. et al., 2018, AJ., 155, 156
Tylenda R., Kamiński T., Schmidt M., Kurtev R., Tomov T., 2011, A&A, 532, A138
Wallerstein G., 1971, ApJ, 169, 195
Werner H. J. et al., 2015, MOLPRO, version 2015.1, a package of ab initio programs, http://www.molpro.net
Werner H.-J. et al., 2020, J. Chem. Phys., 152, 144107
Whiting E. E., Schadee A., Tatum J. B., Hougen J. T., Nicholls R. W., 1980, J. Mol. Spectrosc., 80, 249
Wing R. F., Lockwood G. W., 1973, ApJ, 184, 873
Wing R. F., Spinrad H., Kuhi L. V., 1967, ApJ, 147, 117
Yurchenko S. N., Lodi L., Tennyson J., Stolyarov A. V., 2016, Comput. Phys. Commun., 202, 262
Yurchenko S. N., Al-Refaie A. F., Tennyson J., 2018, A&A, 614, A131
Yurchenko S. N. et al., 2022, MNRAS, 510, 903

SUPPORTING INFORMATION

Supplementary data are available at *MNRAS* online.

Please note: Oxford University Press is not responsible for the content or functionality of any supporting materials supplied by the authors. Any queries (other than missing material) should be directed to the corresponding author for the article.

This paper has been typeset from a TEX/LATEX file prepared by the author.